Molecular engineering to introduce carbonyl between nickel salophen active sites to enhance electrochemical CO_2 reduction to methanol

Zhifu Liang [a,d,1], Jianghao Wang [b,*,1], Pengyi Tang [c,h,1], Weiqiang Tang [g,1], Lijia Liu [e], Mohsen Shakouri [j], Xiang Wang [d], Jordi Llorca [i], Shuangliang Zhao [g,k], Marc Heggen [h], Rafal E. Dunin-Borkowski [h], Andreu Cabot [d,l,**], Hao Bin Wu [f,*], Jordi Arbiol [a,l,**]

[a] Catalan Institute of Nanoscience and Nanotechnology (ICN2), CSIC and BIST, Campus UAB, Bellaterra, 08193 Barcelona, Catalonia, Spain
[b] Institute of Zhejiang University - Quzhou, 78 Jiuhua Boulevard North, Quzhou 324000, China
[c] State Key Laboratory of Information Functional Materials, 2020 X-Lab, Institute of Microsystem and Information Technology, Chinese Academy of Sciences, Shanghai 200050, China
[d] Catalonia Institute for Energy Research – IREC, Sant Adrià de Besòs, Barcelona 08930, Catalonia, Spain
[e] Department of Chemistry, Western University, 1151 Richmond Street, London, ON N6A5B7, Canada
[f] Institute for Composites Science Innovation, (InCSI), School of Materials Science and Engineering, Zhejiang University, Hangzhou 310027, China
[g] State Key Laboratory of Chemical Engineering and School of Chemical Engineering, East China University of Science and Technology, Shanghai 200237, China
[h] Ernst Ruska-Centre for Microscopy and Spectroscopy with Electrons and Peter Grünberg Institute Forschungszentrum Jülich GmbH, 52425 Jülich, Germany
[i] Institute of Energy Technologies, Department of Chemical Engineering and Barcelona, Research Center in Multiscale Science and Engineering, Universitat Politècnica de Catalunya, EEBE, 08019 Barcelona, Catalonia, Spain
[j] Canadian Light Source, Saskatoon S7N 2V3, Canada
[k] Guangxi Key Laboratory of Petrochemical Resource Processing and Process Intensification Technology, School of Chemistry and Chemical Engineering, Guangxi University, Nanning 530004, China
[l] ICREA, Pg. Lluís Companys 23, 08010 Barcelona, Catalonia, Spain

ARTICLE INFO

ABSTRACT

The electrochemical reduction of CO_2 to methanol is a potentially cost-effective strategy to reduce the concentration of this greenhouse gas while at the same time producing a value-added chemical. Herein, we detail a highly efficient 2D nickel organic framework containing a large density of highly dispersed salophen NiN_2O_2 active sites toward electrochemical CO_2RR to methanol. By tuning the ligand environment of the salophen NiN_2O_2, the electrocatalytic activity of the material toward CO_2 reduction can be significantly improved. We prove that by introducing a carbonyl group at the ligand environment of the Ni active sites, the electrochemical CO_2 reduction activity is highly promoted and its product selectivity reaches a Faradaic efficiency of 27% toward the production of methanol at − 0.9 V vs RHE. The salophen-based π-d conjugated metal-organic framework presented here thus provides the best performance toward CO_2 reduction to methanol among the previously developed nickel-based electrocatalysts.

1. Introduction

The electrochemical conversion of carbon dioxide (CO_2) to valuable chemicals using renewable electricity can enable the cost-effective capture and reuse of this greenhouse gas [1,2]. Hydrocarbons and alcohols are the most desired products from the CO_2 reduction reaction (CO_2RR). Among them, methanol is particularly appealing owing to its

numerous uses and its liquid phase at ambient temperature that facilitates storage and transportation. Thus, numerous materials have been explored as CO_2RR catalysts for methanol production, including metal oxides, [3] metal chalcogenides, [4–6] copper-based single atom catalysts, [7,8] small bio-inspired organic molecular catalysts with carbonyl groups [9] two-dimensional metal organic frameworks, [10] or even molecular-based catalysts such as cobalt phtholocyamine anchored on

carbon nanotubes. These former catalysts have been applied for the deep reduction of CO_2 to methanol through domino reduction processes. Their results also exhibited that CO is an important intermediate for the deep reduction of CO_2 to methanol [11,12]. However, despite the relative simplicity of the methanol molecule, the reduction of CO_2 to methanol with high selectivity and stability has been demonstrated extremely challenging and mainly CO and formate have been reported as the CO_2RR products [13–16]. In order to achieve the goal of electro-chemical reduction of CO_2 to methanol, the suitable active sites in the catalysts can not only reduce CO_2 to CO, but also have a suitable binding activity of CO for deep reduction. The weak CO binding activity will lead to the desorption of CO, while the strong binding activity will block the active sites [11,17]. Therefore, designing advanced catalysts with suitable CO binding activity is crucial and challenging for efficient electro-chemical conversion of CO_2 into methanol.

Most of the CO_2RR catalysts developed in the last decades are complex nanomaterials that present unclear structure-performance correlation and uncertain reaction mechanism, which complicates their optimization.[16,18–20]. More recently, molecular catalysts with fine-tuned steric, electronic, electrostatic and chelating properties/abilities [21] have been engineered and optimized (e.g. through ligand modification) for CO_2RR. When supported on conductive substrates, some of these molecular catalysts, such as metalloporphyrin and metallophthalocyanine, cobalt salophen complexes, [22,23] have shown low overpotentials and high CO_2RR conversion efficiency and selectivities [13,24–28]. In the last few years, two-dimensional (2D) conductive metal-organic frameworks with tunable pore structure and functionality, and with abundant catalytic active sites, have arisen as exceptional candidate catalysts for CO_2RR [14,10,29–32]. While several reports have detailed the influence of the metal, ligand type and coordination number on CO_2RR performance, [33,31,34] the analysis and exploitation of the strong influence that the ligand microenvironment near the active center has on the CO_2RR remain unexplored.

Herein, a conjugated nickel organic framework with abundant carbonyl groups in the ligand near the nickel catalytic active site is described and explored as electrocatalyst CO_2RR to methanol in aqueous medium. The unique chemical structure and uniformly distributed catalytic active centers in the proposed nickel organic framework, combined with the high electrical conductivity of carbon nanotubes (CNT), results in electrocatalysts with high catalytic activities, excellent durability and notable selectivity for CO_2RR to methanol. The present work not only provides new insights into the synthesis atomically dispersed material under mild and controllable conditions for electrochemical CO_2 reduction, but also demonstrates a novel strategy to design effective CO_2RR electrocatalysts by tuning the electronic structure through the modification of ligand chemical environment.

2. Experimental section

2.1. Materials

Dimethyl sulfoxide (DMSO), methanol (99.0%), N, N-dimethylformamide (DMF) (98.0%), Dichloromethane (99.0%), salicylaldehyde (99.0%) hydrazine hydrate (98.0%) and 1,2-diaminobenzene (98.0%) were brought from Alfa Aesar. Tetrachloro-p-benzoquinone (99%), N-methyl-pyrrolidone (NMP, 99.99%), potassium phthalimide (98.0%), 1,2,4,5-benzenetetraamine tetrahydrochloride (TAB), 2,5-dimethoxyterephthalaldehyde (97.0%), Nafion (10.0%), hexane (95.0%), Potassium bicarbonate (99.7%) and boron tribromide (99.99%) were purchased from Sigma-Aldrich. Nickel acetate tetrahydrate (99.0%), were from Acros Organics. Acetonitrile (98.0%) and ethanol (99.5%) were purchase from Honeywell. All chemicals were used directly. Carbon Nanotubes (CNTs) was ordered from Sailed Technology in Shenzhen. The oxidation treatment of carbon nanotube (CNTs) was followed in the literature [12].

2.2. Preparation of 2,5-dihydroxyterephthalaldehyde (HBC)

25 mL dichloromethane and 2,5-dimethoxyterephthalaldehyde (250 mg, 1.285 mmol) were placed into 50 mL three-neck flask, then magnetic stirred for 10 min. After that, 3.22 mL BBr_3 (1 M in hexane) was dropped to the above mixture slowly at ice bath. Keep stirring for 3 h at room temperature, then5 mL MILI-Q water was dropped slowly. Then flow argon was used to remove organic solvents and the obtained yellow precipitate was vacuum filtrated and washed with water and acetone several times to obtain a yellow solid with a yield of 75%. (^{1}H NMR (400 MHz, DMSO-d_6, δ)): δ 10.33 (m, 4H), 7.25 (s, 2H) [35].

2.3. Preparation of tetramino-benzenequinone (TABQ)

potassium phthalimide (15 g) and tetrachloro-p-benzoquinone (5.0 g) were put into 100 nL falsk, then acetonitrile (50 mL) were added and magnetically stirred for 12 h at 80 °C. After cooled down to room temperature naturally, the precipitate was filtrated by vacuum, and washed with hot DMF for several times, then washed with MILIQ water and ethanol for several times. Then vacuum dried at 60 °C for overnight. 10.0 g brown-yellow powder of tetra(phthalimido)-benzoquinone was got [36,37]. The obtained tetra(phthalimido)-benzoquinone was transferred into a 100 mL round bottom flask, then 40.0 mL of hydrazine hydrate solution was dropped slowly. After being magnetically stirring and kept at 65 °C for 2 h, the purple tetramino-benzoquinone (TABQ) was obtained with a yield of 26%. (IR -NH2: 3367 cm^{-1}, -C=O: 1668 cm-1, C-(C=O)-C 1140 cm^{-1}) ^{1}H NMR (400 MHz, DMSO-d_6, δ): δ 4.55 (s, 8H) [38,39].

2.4. Preparation of Ni-2D-O-SA and Ni-2D-SA

HBC (166 mg, 1 mmol), TABQ (84 mg, 0.5 mmol), nickel acetate tetrahydrate (1 mmol, 248.8 mg) and 5 mL NMP were placed into a 15 mL glass vial, The obtained mixture was sonicated for 30 min to form a homogenous dispersion. The glass vial was put into a 25 mL Teflon-lined stainless-steel autoclave. The autoclave was sealed and maintained at 120 °C for 72 h. The obtained black precipitate was filtrated and then washed with DMF and methanol for several times, Soxhlet extracted by methanol for 24 h, then dried under vacuum at 60 °C for 24 h to give a black powder with ~83% yield ($C_{11}N_2O_3NiH_4$.2 H_2O, Elemental Analysis, calculated: C, 43.05; H, 2.63; N, 9.13; Found: C, 42.04; H, 3.14; N, 8.36).

The preparation procedure of Ni-2D-SA is similar as Ni-2D-O-SA, the precursor TABQ was replaced by 1,2,4,5-benzenetetraamine tetrahydrochloride (TAB) [40]. ($C_{11}N_2O_2NiH_5$·H_2O elemental analysis Calculated: C, 48.24; H, 2.58; N, 10.23; Found: C, 47.34; H, 3.24; N, 9.26).

2.5. Preparation of Ni-2D-O-SA-CNT and Ni-2D-SA-CNT composites

30 mg Ni-2D-O-SA, 5 mL NMP and 70 mg pre-oxidized carbon nanotubes (CNTs) were added into a 15 mL glass vial. The obtained mixture was sonicated for half an hour, and stirred at 100 °C for 12 h, The obtained black composite was collected by vacuum filtration and washed with ethanol for several times, and then vacuum dried at 60 °C for 24 h.

Ni-2D-SA-CNT composites were synthesized by using the same procedure as for Ni-2D-O-SA-CNT, just the precursor of Ni-2D-SA was replaced by Ni-2D-O-SA.

2.6. Preparation of model complex Ni-salophen (Ni-SA)

First, the salophen ligand was synthesized by placing 108 mg (1 mmol) of 1,2-diaminobenzene in 15 mL three-neck flask. Then 6 mL Ethanol were added and the mixture was heated to 70 °C under stirring, after that, 2 mmol of salicylaldehyde were added to the above mixture. The mixture was refluxed for 24 h. After cooling to room temperature,

the obtained precipitates were vacuum filtrated and washed with EtOH for several times. Finally, the yellow powder was dried under vacuum at 60 °C overnight. To prepare the Ni-salophen (Ni-SA), 60 mg of Ni $(CH_3COO)_2 \cdot 4H_2O$, 90 mg of salophen ligand and 6 mL of MeOH were put into a 15 mL flask. The obtained mixture was heated to 60 °C with

$$\text{Relative peak area ratio(methanol)} = \frac{\text{singlet peak area at 3.23ppm(methanol)}}{\text{singlet peak area at 2.6ppm(DMSO)}}$$

magnetic stirring for one day under argon. The mixture was filtrated by vacuum and washed with MeOH for several times. Finally, the reference complex Ni-SA was dried under vacuum at 60 °C overnight.

2.7. Working electrode preparation

1 mg of catalyst was dispersed in the mixture of isopropanol (475 μL) and Nafion (5%, 25 μL) by sonication for 1 h to obtain uniformly inks. Then, the inks were dropped on the carbon paper (1 * 1 cm^2) under the infrared grill light. After dropping, the electrodes were further dried by infrared grill light at least 20 min before test.

2.8. Electrochemical measurements

All electrochemical measurements were performed in a gas-tight H-type glass cell containing a Nafion 117 membrane using a Biologic VMP3 multichannel potentiostat workstation at room temperature. The electrolyte (0.1 M $KHCO_3$) was saturated with CO_2 before each experiment by bubbling CO_2 for 20 min. In a typical three-electrode test system, a graphite rod and an Ag/AgCl electrode were used as the counter electrode and the reference electrode, respectively. All working electrodes were dried by infrared grill light at least 20 min before test. Each fresh sample was measured with a chronoamperometric step for 1 h at each potential. The roughness factors were determined by measuring the double-layer capacitance with cyclic voltammetry in the potential range of open circuit potential ± 50 mV at varying scan rates (2, 5, 10, 20, 50, 100 mV s^{-1}). All potentials were converted to the RHE using the relationship: E(RHE) = E(Ag/AgCl) + 0.197 + 0.059 *pH [41]. The pH of 0.1 M $KHCO_3$ saturated with CO_2 is 6.8, which is measured by a pH-meter. The potentiostat workstation was set to compensate 85% of the ohmic drop, and no further iR correction was performed.

During electrolysis, CO_2 gas (99.995%) was delivered into the cathodic compartment containing CO_2-saturated electrolytes at a rate of 20 sccm and vented into online gas chromatography (GC) equipped with a combination of molecular sieve 5 A. Methane and carbon monoxide were detected by a methanizer-flame ionization detector, and the hydrogen was detected by a thermal conductivity detector. Every 20 min, 1 mL of gas was sampled to determine the concentration of gaseous products. After electrolysis, the liquid products in catholyte were quantified by Nuclear Magnetic Resonance (NMR). Specifically, 500 μL of catholyte was taken out after 1 h of CO_2 electroreduction. It was then mixed with 150 μL of internal standard. The internal standard was obtained by dissolving 2.5 mM Dimethyl sulfoxide (DMSO) into D_2O solvent. After that, the mixture was then transferred into a NMR sample tube for measurement.

The $FE_{methanol}$ was calculated by the following formula:

$$FE\text{methanol} = \frac{C_{methanol} \times V \times N_A \times 6e}{N_{total}}$$

Where $C_{methanol}$ is the concentration of methanol in the electrolyte, V is the volume of electrolyte, N_A is Avogadro's constant, N_{total} is the total number of electrons measured during the entire CO_2RR.
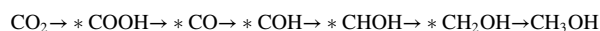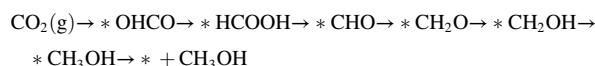
The concentration of methanol ($C_{methanol}$) was obtained using the calibration curves shown in Fig. S13. The calibration curves were made by measuring standard solutions of methanol.

The peaks were quantified by integrating the area. the relative peak area can be calculated as follows:

2.9. Density functional theory (DFT) calculations

All the data were calculated from density functional theory (DFT) by the Vienna ab initio Simulation Package (VASP) [42,43]. The generalized gradient approximation of Pardew-Burke-Ernzerhof (PBE) method with van der Waals correlation was conducted to optimize the geometric structures [44]. The convergence criteria was 0.05 eV/Å in force and 1×10^{-5} eV in energy, while the plane wave cutoff was 500 eV. The Monkhorst-Pack mesh k-point grids was $1 \times 1 \times 1$ for all models. All of the vacuum thicknesses were higher than 15 Å.

The whole process of CO_2 electrochemical reduction to methanol for comparison we choose consists the following steps:

$$CO_2(g) \rightarrow *OHCO \rightarrow *HCOOH \rightarrow *CHO \rightarrow *CH_2O \rightarrow *CH_2OH \rightarrow$$
$$*CH_3OH \rightarrow * + CH_3OH$$

$$CO_2 \rightarrow *COOH \rightarrow *CO \rightarrow *COH \rightarrow *CHOH \rightarrow *CH_2OH \rightarrow CH_3OH$$

Where the * and *OHCO represent free sites and the adsorption state of OHCO, respectively. The (g) represent the gas phase.

The adsorption energy was calculated by

$$\Delta E = E_{total} - E_{surface} - E_{adsorbents}$$

where E_{total}, $E_{surface}$, and $E_{adsorbents}$ are the DFT-calculated energy for total system, pure surface, and pure adsorbents, respectively.

The reaction free energies of each step were calculated by the following formula:

$$\Delta G = \Delta E + \Delta E_{ZPE} - T\Delta S$$

where ΔE_{ZPE} is the zero-point energy, $T\Delta S$ (T = 298.15 K) is the entropy contribution.

2.10. Characterizations

The crystal structure of the materials was characterized by means of powder X-ray diffraction (XRD) measured in a Bruker AXS D8 Advance X-ray diffractometer. (Cu-Kα radiation, λ = 1.5106 Å, 40 kV and 40 mA; Bruker, Germany). ^{13}C cross-polarization with magic angle-spinning (CP-MAS) solid-state nuclear magnetic resonance (NMR) spectra were measured on a Bruker ARX 400 MHz spectrometer. Thermogravimetric analysis (TGA) was performed under air and nitrogen gas at a heating rate of 5 °C/min using a Thermogravimetric Analyzer Q200. Scanning electron microscopy (SEM) images were obtained in a Zeiss Auriga Field emission scanning electron microscope (FE-SEM) operating at 20 kV. High-resolution transmission electron microscopy (HRTEM) studies were conducted in a FEI Tecnai F20 microscope at an operating voltage of 200 keV. High angle annular dark-field (HAADF)-scanning transmission electron microscopy (STEM) images and elemental mapping were measured in a spherical aberration corrected transmission electron

microscope FEI Titan G2 80–200 ChemiSTEM with four energy-dispersive X-ray spectroscopy (EDX) detectors and operated at 80 and 200 keV. X-ray photoelectron spectroscopy (XPS) data was obtained with a Phoibos 150 MCD-9 detector. The Ni K-edge X-ray absorption fine structure (XAFS) spectra were measured at the Canadian Light Source, beamline SXRMB. The samples were pressed onto a double-sided carbon tape and the data was recorded in X-ray fluorescence mode. The XAFS data was processed with the Athena program [45]. Extend X-ray absorption fine structure (EXAFS) was analyzed using the IFEFFIT package [46] and the EXAFS fitting was performed with FEFF6L [47]. For EXAFS fitting, spectra were fitted in R-space, from 1.0 Å to 2.76 Å. The R-space EXAFS signal was obtained by a variable k^n-weighted Fourier transform (n = 1, 2, 3) of the EXAFS signal $\chi(k)$ over a k-range of 3.00 Å^{-1} to 11.7 Å^{-1}. The coordination numbers of Ni-N and Ni-O paths were both fixed at 2, and the bond lengths, energy shift, and the Debye-Waller factors were optimized to yield the best fit. Nitrogen adsorption-desorption isotherms were recorded in a Tristar II 3020 Micromeritics system at 77 K. The specific surface area was calculated by Brunauer–Emmett–Teller (BET) method.

3. Results and discussions

3.1. Structure characterizations

As shown in Scheme 1, the targeted 2D nickel organic framework (Ni-2D-O-SA) with abundant carbonyl functional group was solvothermally synthesized by a Schiff-based reaction between 2,5-hydroxyterephthalaldehyde (HBC), nickel acetate and tetramino-benzoquinone (TABQ) in N-methyl-2-pyrrolidone (NMP). The dark-black precipitate obtained from this reaction indicated the formation of a conjugated polymer. This precipitate was vacuum filtrated, washed with water and methanol to remove small molecular mass impurities and finally dried under vacuum at 60 °C. A control sample, without the carbonyl chemical groups (Ni-2D-SA), was prepared using the same reaction process and conditions but replacing TABQ by 1,2,4,5-benzene-tetraamine tetrahydrochloride (TAB) (Fig. S1) [40].

The Ni-2D-O-SA powder exhibited a crystalline and layered structure, as observed by powder X-ray diffraction (XRD) analysis (Fig. S2). The Ni-2D-O-SA XRD pattern was similar to that of graphite, with a diffraction peak at 26.29° corresponding to the (001) family planes, and thus indicating π-π layered stacking.[48] In contrast, the XRD pattern of the control sample, Ni-2D-SA, displayed a much lower crystallinity. This result indicates that the introduction of the carbonyl groups enhances the crystallinity of the nickel organic frameworks through π-π interaction.

The Fourier transform infrared (FT-IR) spectra (Fig. S3) of the two samples displayed the footprint of C=N at 1642 cm^{-1} for Ni-2D-SA and 1648 cm^{-1} for Ni-2D-O-SA. At the same time, the characteristic peaks of the N-H stretching vibration (3367–3197 cm^{-1}) disappeared. These pieces of evidence demonstrated the completion of the Schiff-based reaction and the formation of Ni-salophen structure units [40]. The vibration of the carbonyl group (C=O) in Ni-2D-O-SA negatively shifted below 1600 cm^{-1}, where it overlapped with other vibrations. Besides, the vibration peak for the C-(C=O)-C bond in Ni-2D-O-SA, which is

Ni-2D-SA
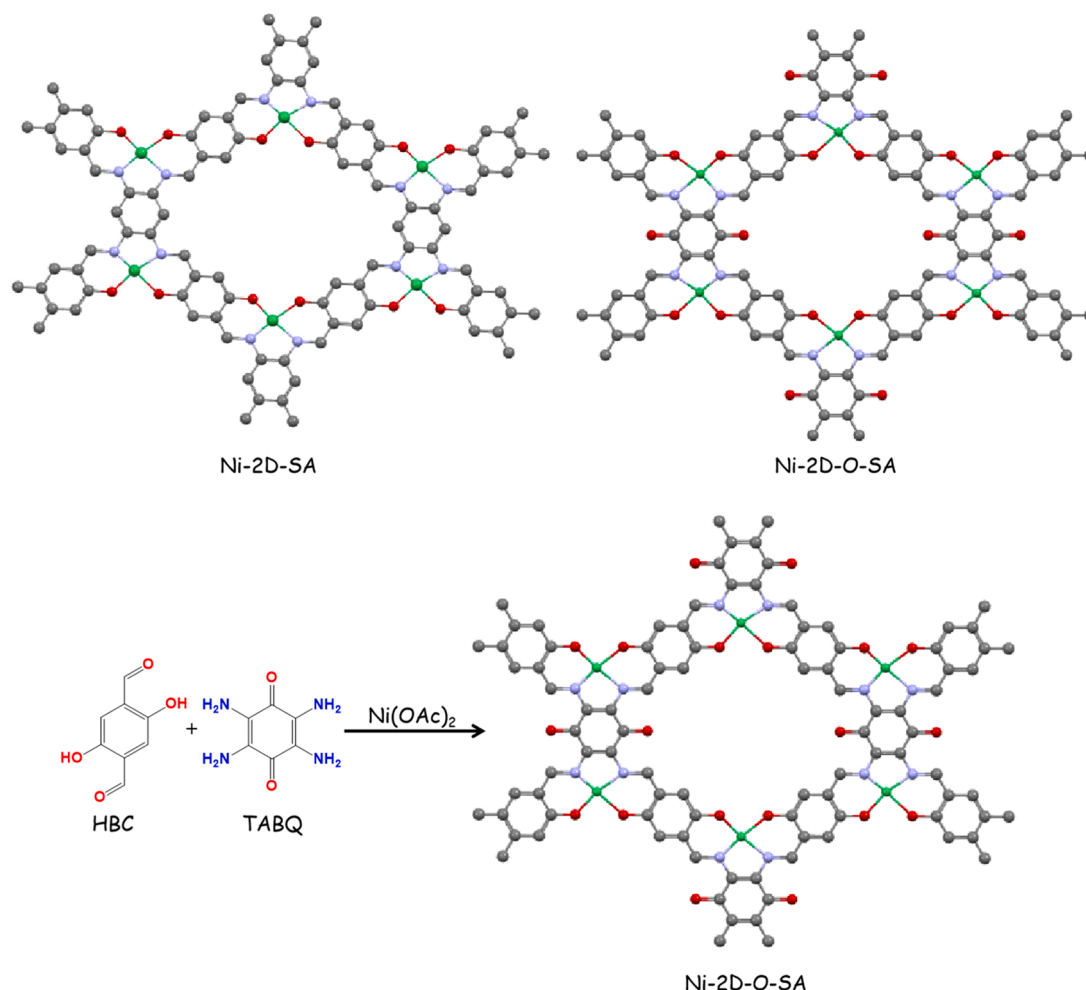
Ni-2D-O-SA

Ni-2D-O-SA

Scheme 1. Schematic representation of the synthesis of Ni-2D-O-SA (blue corresponds to nitrogen, red to oxygen, green to nickel and grey to carbon).
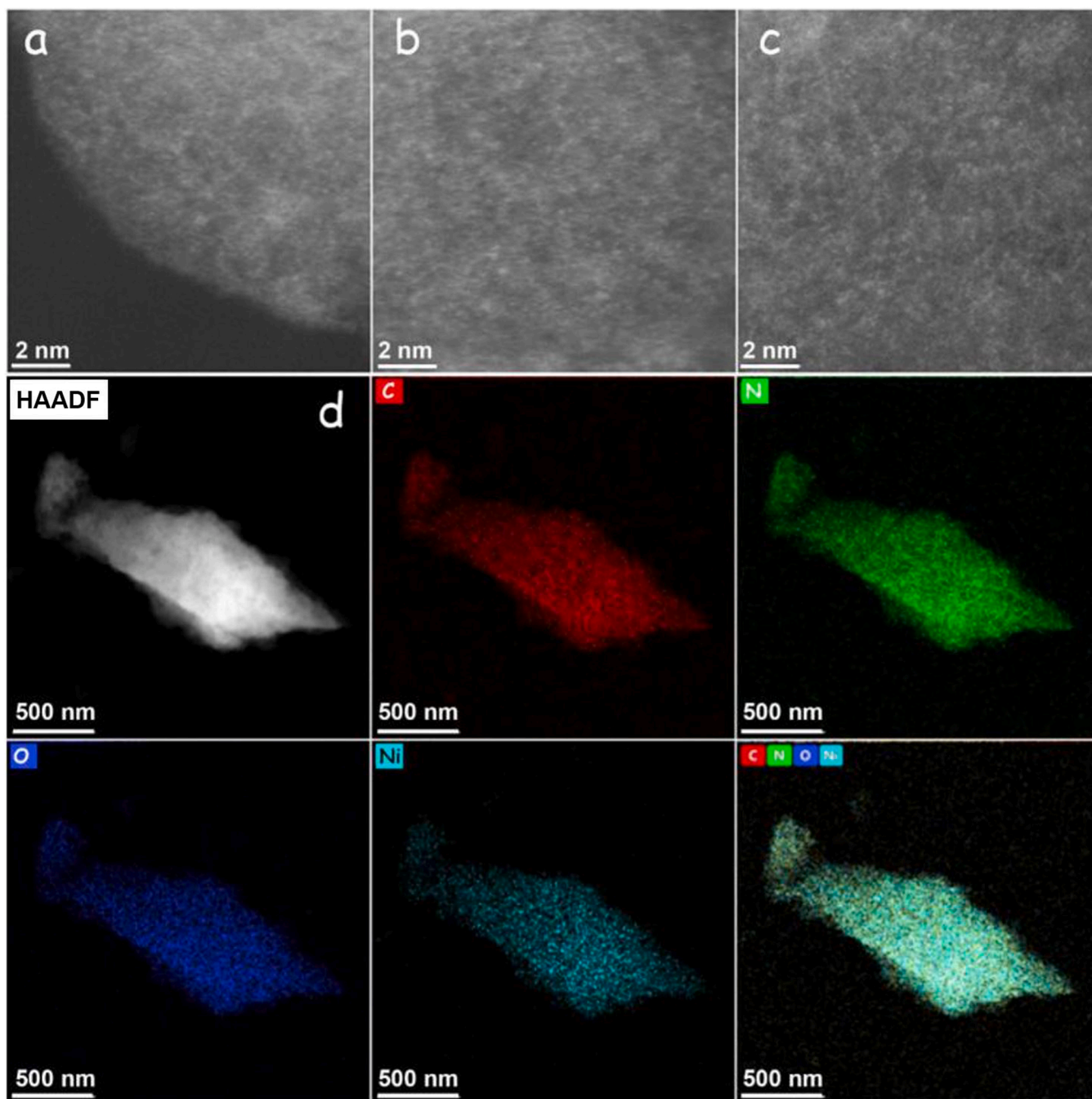
Fig. 1. (a)–(c) HAADF-STEM images of Ni-2D-O-SA displaying atomically dispersed nickel atoms as brighter spots in the image. (scale bar with 2 nm) (d) Low magnification HAADF-STEM image and EDS elemental maps for C (red), Ni (light blue), N (green) and O (blue) (scale bar with 500 nm).

characteristic of the TABQ, shifted from 1140 cm^{-1} to 1010 cm^{-1} due to the coordination effect and the attraction between the layers. These results demonstrated the formation of the organic framework containing the carbonyl groups [49]. The solid-state ^{13}C CP/MAS NMR spectrum of the Ni-2D-O-SA catalyst exhibits the presence of C=O, C=N, C=C, with the corresponding signals at 160 ppm, 149 ppm and 123 ppm, respectively. Instead, for the Ni-2D-SA catalyst, the resonance signals of C=N and C=C appear at 150 ppm and 120 ppm, respectively (Fig. S4).

Ni-2D-O-SA displayed a very porous morphology, resembling that of cotton when analyzed by scanning electron microscopy (SEM) (Figs. S5a). High angle annular dark-field (HAADF)-aberration-corrected scanning transmission electron microscopy (STEM) analysis (Fig. 1a–c and Fig. S6) demonstrated the presence of a high density of

atomically dispersed and homogeneously distributed nickel atoms. The energy-dispersed X-ray spectroscopy (EDS) elemental mapping shown in Fig. 1d further demonstrated the uniform distribution of Ni, C, N, and O.

The Brunauer-Emmett-Teller surface areas of Ni-2D-O-SA and Ni-2D-SA were calculated at 21 and 83 m^2 g^{-1}, respectively [50]. Thus the presence of the carbonyl functional group decreases the surface area of the material, which is consistent with the higher π-π driven organization of the two dimensional Ni-2D-O-SA framework observed by XRD analysis. The pore size distribution profiles (Fig. S10) show the approximate porous structures of Ni-2D-SA and Ni-2D-O-SA.
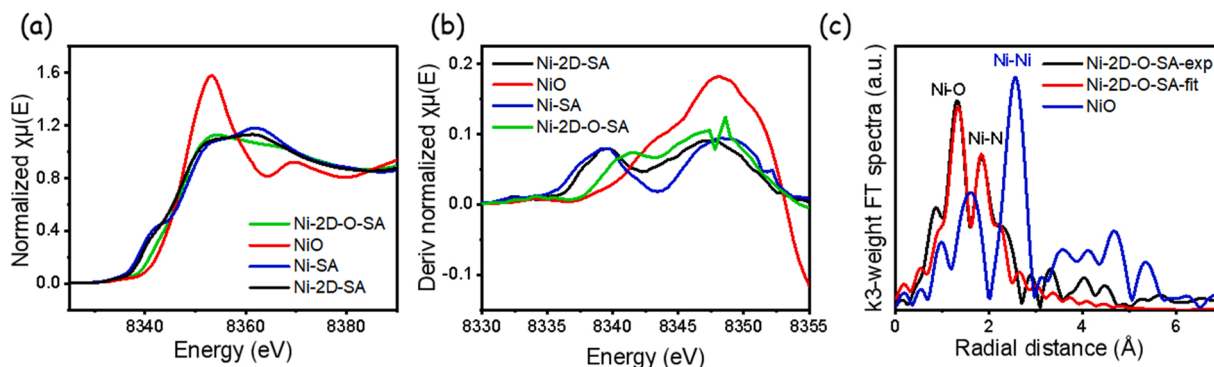
Fig. 2. (a) Ni K-edge XANES spectrum of Ni-SA, Ni-2D-SA, Ni-2D-O-SA and NiO (commercial powder), (b) First derivative of the Ni K-edge XANES for Ni-SA, Ni-2D-SA, NiO and Ni-2D-O-SA. (c) Fourier transformed Ni K-edge EXAFS spectra of Ni-2D-O-SA and NiO plotted in R-space, Fourier transformed EXAFS spectra in R-space of Ni-2D-O-SA and fitted curve.

3.2. Fine structure of Ni-2D-O-SA and Ni-2D-SA

To further confirm the local coordination environment of Ni active sites in Ni-2D-O-SA, XAFS analysis of the Ni K-edge was conducted (Fig. 2a-b). We first compared the spectral features of Ni-2D-O-SA with those of Ni-2D-SA, NiO, and a model complex Ni-salophen (Ni-SA) at the near-edge (i.e. X-ray absorption near-edge structure, XANES). As shown in Fig. 2a, the absorption energy of near K-edge in XANES spectrum for the Ni-2D-O-SA sample shifted to higher energy compared to that of Ni-2D-SA, which suggests that the introduction of carbonyl groups resulted in a higher oxidation state of the Ni active centers. The absorption onset of Ni-2D-O-SA occurs at slightly lower energy than that of NiO. Differences are more clearly seen when the first derivative of these spectra are plotted (Fig. 2b). The main absorption peak of Ni-2D-O-SA also has a lower intensity. These features indicate that, compared with NiO where Ni is fully coordinated with O, Ni atoms within Ni-2D-O-SA are surrounded by less electronegative elements, i.e. N substituting O. The EXAFS spectrum was analyzed to obtain more quantitative details of the coordination environment. First the EXAFS spectrum of Ni-SA was fitted well with a NiN_2O_2 coordination structure (Fig. S7 and Table S1), the Ni-2D-SA was also fitted with a NiN_2O_2 coordination structure (Fig. S8 and Table S2). The Fourier transformed EXAFS of Ni-2D-O-SA is shown in Fig. 2c. The fitted curve suggests that Ni is coordinated with two N atoms and two O atoms, at a bond length 1.87 Å and 2.05 Å, respectively (Fig. 2c), which matches well the salophen unit structure (NiO_2N_2). The contribution at longer radial distances comes from C atoms with a co-ordination number of 6 and a bond length of 2.65 Å, which also belong to the Ni.C interaction (Table S3) and the distance of Ni.Ni interaction is of 3.168 Å which corresponds to the Ni in the layer-layer structure for this type of materials. Thus, the XAFS analysis confirmed the formation of the NiN_2O_2 salophen structure unit within Ni-2D-O-SA frameworks. To confirm the coordination structure stability of Ni-2D-O-SA, the EXAFS spectrum of Ni-2D-O-SA which was immersed in a $KHCO_3$ aqueous solution for three days was fitted (Fig. S9 and Table S4). The Ni-2D-O-SA maintained the NiN_2O_2 coordination structure, indicating its structure stability in the $KHCO_3$ aqueous solution.

3.3. CO2RR activity

To promote the electrical conductivity of the nickel-based organic frameworks toward their use as efficient electrocatalysts, they were supported on multi-walled CNTs by physical mixing in dimethylformamide. XRD patterns displayed just one broad diffraction peak at about 26° (Fig. S11), which was assigned to the overlap between the CNT and the nickel organic framework structures. The porous morphology and the homogenous loading of Ni-2D-O-SA on the CNTs within the obtained composites (Ni-2D-O-SA-CNT) were confirmed by STEM images and EDS elemental mapping (Fig. S12).

The electrocatalytic properties of Ni-2D-O-SA-CNT toward CO2RR were tested in a two-compartment electrochemical cell containing a CO2-saturated 0.1 M $KHCO_3$ electrolyte. As shown in Fig. 3a, the Ni-2D-O-SA-CNT catalyst displayed higher current densities in the CO2-saturated electrolyte than in Ar-saturated electrolyte at potentials more positive than − 0.9 V vs RHE, which indicates a clear CO2RR activity. When the applied potentials were more negative than − 0.9 V, the current density in a CO2-saturated electrolyte was lower than in the Ar-saturated electrolyte due to the HER suppression through CO2 adsorption. The liquid products of CO2RR was analyzed by ^{1}H NMR (Fig. S14).

Ni-2D-O-SA-CNT samples displayed much higher current densities than Ni-2D-SA-CNT under the same test conditions (Fig. 3b and Fig. S15a-b), which demonstrates that Ni-2D-O-SA-CNT has better activity toward CO2RR than that of Ni-2D-SA-CNT. Given that Ni-2D-O-SA-CNT and Ni-2D-SA-CNT were characterized by similar electrochemical double-layer capacitances (Fig. S16), we can conclude that the presence of the carbonyl group within Ni-2D-O-SA organic framework decisively increases its CO2RR activity.

The CO2RR product distribution obtained from Ni-2D-O-SA-CNT and Ni-2D-SA-CNT electrocatalysts at different potentials was evaluated by gas chromatography and nuclear magnetic resonance. The Faradaic efficiency of all products are provided in Figs. S15c and S15d, which show that H_2 is one of the CO2RR products, too. The Methanol faradaic efficiency was quantified by liquid NMR technology. As shown in Fig. 3c, Ni-2D-O-SA-CNT is characterized by a volcano-shaped Faraday efficiency (FE) and partial current densities toward CH_3OH in the range of applied potential from − 0.85 to − 1.05 V. The maximum CH_3OH FE of 27% and j_{MeOH} of 0.94 mA cm^{-2} were achieved by Ni-2D-O-SA-CNT at − 0.9 and − 0.95 V vs. RHE, respectively. This excellent performance is in contrast with the nickel organic framework without the carbonyl group Ni-2D-SA-CNT (9.2% FE for CH_3OH at −0.95 V, Fig. 3d). The high performance of Ni-2D-O-SA-CNT is also in contrast with all previously developed nickel-based CO2RR catalysts, which mostly yielded CO instead of methanol (Table S5) [24,33]. To the best of our knowledge, only one previous report demonstrated CO2RR to methanol using a Ni-based electrocatalyst but with a moderate activity and selectivity (6% FE) [10]. Compared with Ni-2D-SA-CNT, in the potential range from − 0.85 to − 1 V Ni-2D-O-SA-CNT also exhibited a higher selectivity toward the production of CO, which is an intermediate in the production of methanol (Fig. 3e) [7,11,12].

To exclude the possibility that the formation of methanol came from the preparation process or the decomposition of the catalyst, we analyzed the product distribution of the Ni-2D-O-SA-CNT sample in Ar-saturated 0.1 M $KHCO_3$. The obtained results showed that no methanol signal could be found, and that the Ni-2D-O-SA-CNT catalyst could only produce hydrogen in Ar-saturated 0.1 M $KHCO_3$ (Figs. S17 and S18). These results demonstrate the excellent intrinsic catalytic selectivity toward methanol of the Ni-2D-O-SA-CNT sample.
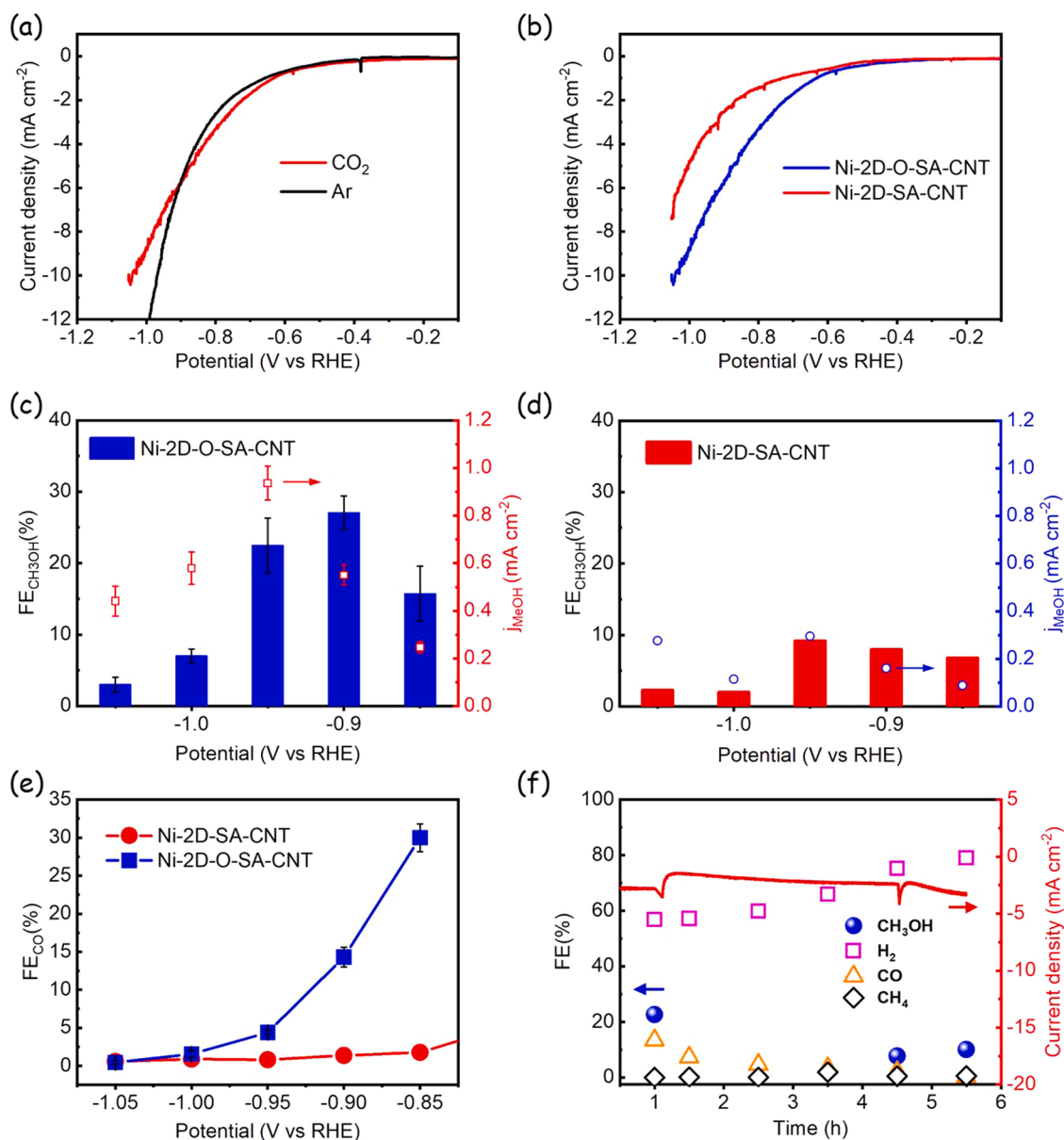
Fig. 3. Electrocatalytic CO_2RR performance of Ni-2D-O-SA-CNT and Ni-2D-SA-CNT. (a) Linear sweep voltammetry (LSV) curves of Ni-2D-O-SA-CNT at a scan rate of 5 mV s^{-1} in CO_2- and Ar-saturated 0.1 M KHCO$_3$ electrolytes. (b) LSV curves of Ni-2D-O-SA-CNT and Ni-2D-SA-CNT in CO_2-saturated 0.1 M KHCO$_3$ electrolyte. (c,d) FEs and current densities of Ni-2D-O-SA-CNT (c) and Ni-2D-SA-CNT (d) toward CH$_3$OH at various applied potentials, from $-$ 0.85 to $-$ 1.05 V. (e) CO$_2$ to CO FE of Ni-2D-O-SA-CNT and Ni-2D-SA-CNT at various applied potentials from $-$ 0.85 to $-$ 1.05 V vs RHE. (f) Current-time (*i-t*) responses and corresponding FEs of Ni-2D-O-SA-CNT at $-$ 0.9 V vs RHE for 5.5 h.

The catalytic stability of Ni-2D-O-SA-CNT was evaluated at $-$ 0.85 V vs RHE (Fig. 3f). We observed the current density to be maintained during an operating period of 5.5 h. Although the selectivity of methanol is decreased after a relatively long electrochemical test, the Ni-2D-O-SA-CNT catalyst could still maintain ~10% FE toward methanol.

To understand which are the real active sites for the formation of methanol and the reason of deactivation after the long-term stability test, we analyzed the post reaction sample by XRD, FT-IR, and XPS. From XRD patterns (Fig. S20a), the characteristic peaks of Ni-2D-O-SA-CNT are well maintained after CO$_2$RR test, and no presence of other peaks was observed, suggesting that no Ni-based metal or metal oxide nanoparticles were formed. XPS was further conducted to investigate the electronic structure of Ni after CO$_2$RR (Fig. S21). We found that only a small Ni2p3/2 signal remained after the CO$_2$RR test, indicating a partial decomposition of the NiN$_2$O$_2$ sites, which would be responsible for the deactivation of our catalyst. This residual Ni2p3/2 signal is still

maintained at 855.5 eV after the CO$_2$RR test, indicating that the active sites for methanol formation can still be Ni species with 2+ valence. In addition, there is no presence of metallic nickel in the XPS spectra. The FT-IR spectra showed that the carbonyl groups of Ni-2D-O-SA-CNT were still maintained after the long-term stability test, implying that the carbonyl groups were not lost (Fig. S20b). To further demonstrate the effect of the Ni sites on the formation of methanol, we also evaluated the CO$_2$RR performance of the 2D-O-SA-CNT catalyst (without nickel) at the same potentials. The results show that almost all products obtained by 2D-O-SA-CNT are hydrogen instead of CO$_2$RR related products (Fig. S22), demonstrating the importance of the Ni active sites for the formation of methanol. Moreover, the selectivity of methanol decreased with the decay of NiN2O2, implying a positive correlation between the selectivity of methanol and the amount of NiN2O2. Therefore, the residual NiN2O2 sites still found in the sample after the 5 h test were responsible for the still kept methanol selectivity. The degradation of

methanol selectivity and Ni XPS signals is because the Ni-2D-O-SA that are not directly loaded on carbon nanotubes (CNTs) are less stable compared to those directly attached to the CNTs through π-π stacking interactions. Namely, those nanolayers directly attached to the CNT surface, highly improve their physical and chemical robustness [26]. Normally, molecular catalysts can be anchored on the surface of the carbon nanotube through the π-π stacking interaction, which facilitates the electron transfer and prevent gathering of the active sites to improve the physical and chemical stability [33]. Unlike the small molecular catalysts, Ni-2D-O-SA is a two-dimensional organic material, which can also promote the π-π stacking interaction between its layers and the CNTs. Therefore, it is hard to guarantee that all these Ni-2D-O-SA 2D nanostructures are loaded on the surface of CNTs with their single layers promoting the π-π stacking interaction. In this way, those Ni-2D-O-SA nanolayers that are not directly loaded on the surface of a CNT would not present any π-π stacking interaction and thus, they would not be as stable during the CO2RR process, resulting in the decomposition of these Ni-2D-O-SA nanolayers and the corresponding degradation of the catalytic performance.

Both electrocatalysts, Ni-2D-O-SA-CNT and Ni-2D-SA-CNT yielded methanol with a significant FE, which indicates that the porous structure, the high densities of nickel active centers, and possibly the short distance between the catalytic active sites are highly suitable for the electroreduction process of CO_2 to methanol. Furthermore, the presence of the carbonyl group in the ligand between the nickel active centers in the Ni-2D-O-SA-CNT electrode resulted in a very notable enhancement of the FEs for CO_2 reduction to both methanol and CO. Thus, the presence of the carbonyl group clearly favors the electroreduction of CO_2 to CO, which can be considered as a first step in the formation of methanol. But at the same time, this carbonyl group promotes a deepen electrochemical reduction, which we tentatively attribute to the stronger π-d conjugation that enhances the adsorption of the intermediates generated in the electrochemical reduction process of CO_2 to methanol over the nickel active centers [12,51]. The strong electronegativity of the carbonyl group could shift the electron cloud in nickel active centers (NiN_2O_2), resulting in a more positive valence of the Ni sites in Ni-2D-O-SA, and thus promote the conversion of CO_2 into CO, [52]. This higher valence has been reported to promote a deeper CO_2 electroreduction in different metals [53].

3.4. Mechanic study

To further understand the effect of the carbonyl group, the differential charge distribution was estimated by density functional theory (DFT) calculations. The electron density difference between of Ni-2D-SA and Ni-2D-O-SA (Fig. 4a) illustrates that the charge transfer from Ni ion to ligand appears, which is due to the inductive effect of carbonyl group in Ni-2D-O-SA. This results are consistent to the XANES analysis, which show that the Ni center in Ni-2D-O-SA has a higher oxidation state compared to that of Ni-2D-SA. The absolute free energy of H* on Ni-2D-
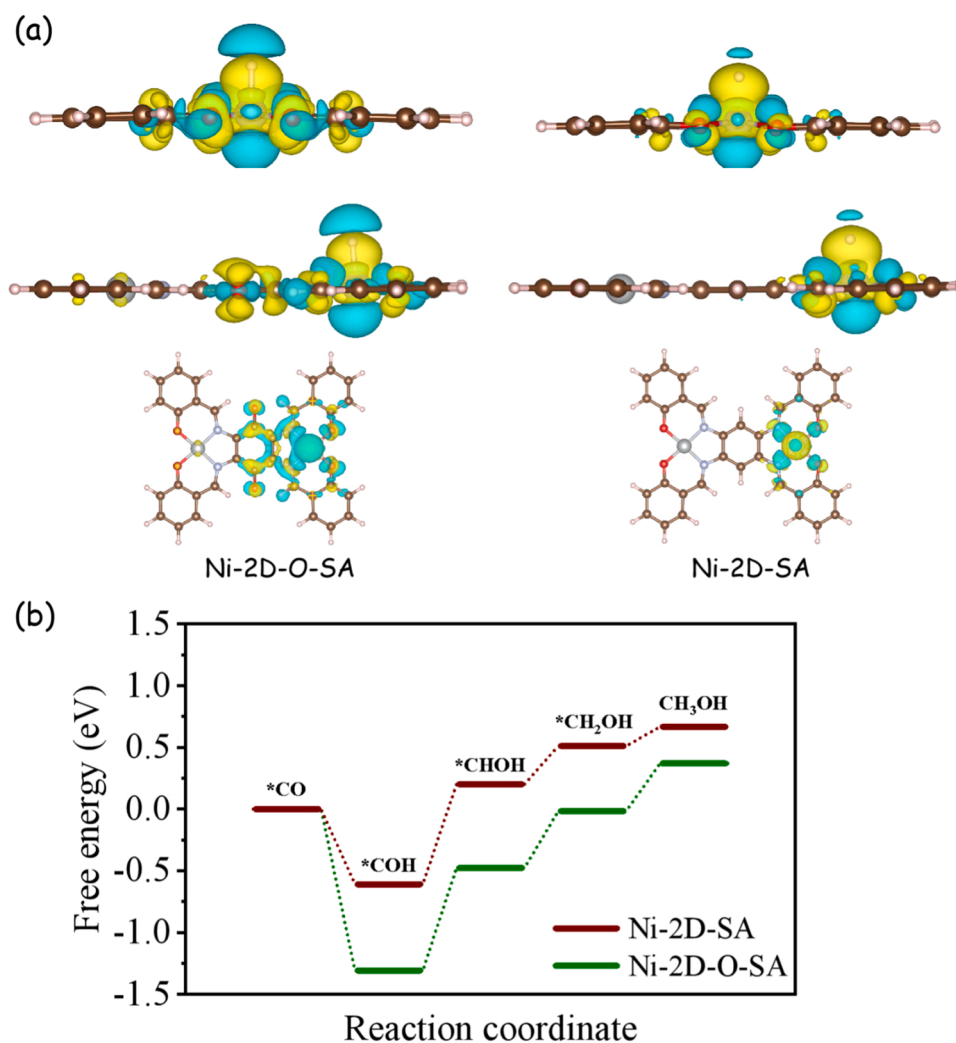
Fig. 4. (a) Plots of electron density difference for selected segments of Ni-2D-O-SA and Ni-2D-SA. The yellow color corresponds to an isosurface of 0.00120794 e Bohr^{-3} and blue of $-$ 0.00120794 e Bohr^{-3}. (b) Free energy diagram of *CO to CH_3OH on selected segments of Ni-2D-O-SA.

O-SA is larger than that of Ni-2D-SA, suggesting that the Ni-2D-SA catalyst is more favorable for hydrogen evolution reaction (HER) (Fig. S23). Further more, the free energy diagram in the conversion from *CO to methanol was calculated, and the reaction pathway was proposed based on the previous report [7]. According to our DFT calculation results (Fig. 4b), the conversion of *CO to methanol is thermodynamically more favorable on Ni-2D-O-SA than that on Ni-2D-SA. The result of the adsorption energy for intermediates (Fig. S24) further confirms that the introduction of the carbonyl group in Ni-2D-O-SA will favor the adsorption of the intermediates compared with Ni-2D-SA. On the other hand, a second reaction pathway of the conversion from CO_2 to methanol based on another published work [8] was also calculated. As exhibited in Fig. S25, the free energy in the rate-determining step of the conversion of *OHCO to absorbed *HCOOH is lower on Ni-2D-O-SA. Therefore we can suggest that Ni-2D-O-SA with carbonyl groups would tend to favor the electrocatalytic reduction of CO_2 to methanol with respect to Ni-2D-SA.

4. Conclusion

We have detailed the synthesis and characteristics of an atomically dispersed nickel catalyst consisting of NiN_2O_2 active sites within a 2D organic framework under mild and controllable reaction condition. A molecular engineering strategy based on modifying the edge ligand environment by introducing a carbonyl group was proposed to tune the electrocatalytic reduction of CO_2. The obtained Ni-O-SA-CNT composites exhibited excellent activity and selectivity (27% FE at -0.9 V vs RHE) toward the conversion of CO_2 to methanol due to the carbonyl group was introduced in the ligand environment to tune the electronic structure of the nickel active sites. This work not only provides the best nickel-based catalysts so far reported for the electrocatalytic conversion of CO_2 to methanol, but also demonstrates a novel strategy to design and engineer efficient electrocatalysts to convert CO_2 to valuable chemicals through modulating the ligand structures.

CRediT authorship contribution statement

Zhifu Liang: equally contributed to this work, synthesized the catalysts and finish the basic characterizations and wrote the paper. **Jianghao Wang:** equally contributed to this work, performed the catalytic test. **Pengyi Tang:** equally contributed to this work, conducted the AC-STEM analysis. **Weiqiang Tang:** equally contributed to this work, conducted DFT calculation. **Lijia Liu:** conducted the XAFS analysis. **Mohsen Shakouri:** conducted the XAFS analysis. **Xiang Wang:** performed the SEM measurements. **Jordi Llorca:** conducted XPS analysis. **Andreu Cabot:** Funding acquisition, Project administration, Resources, Writing – review & editing. **Hao Bin Wu:** Funding acquisition, Project administration, Resources, Writing – review & editing. **Jordi Arbiol:** Funding acquisition, Project administration, Resources, Writing – review & editing. All authors discussed the results and commented on the manuscripts.

Declaration of Competing Interest

The authors declare the following financial interests/personal relationships which may be considered as potential competing interests: Jordi Arbiol reports financial support was provided by Spanish MINECO. Jordi Arbiol reports financial support was provided by Government of Catalonia. Jordi Arbiol reports financial support was provided by Horizon 2020. Jordi Arbiol reports financial support was provided by MCIN. Jordi Llorca reports financial support was provided by European Regional Development Fund. Xiang Wang reports financial support was provided by China Scholarship Council. PengYi Tang reports financial support was provided by Humboldt Research Fellowship. Lijia Liu reports financial support was provided by Natural Sciences and Engineering Research Council Canada. Mohsen Shakouri reports financial

Appendix A. Supporting information

Supplementary data associated with this article can be found in the online version at doi:10.1016/j.apcatb.2022.121451.

References

[1] O.S. Bushuyev, P. De Luna, C.T. Dinh, L. Tao, G. Saur, J. van de Lagemaat, S. O. Kelly, E.H. Sargent, What should we make with CO_2 and how can we make it? Joule 2 (2018) 825–832.

[2] L. Zhang, Z.J. Zhao, J. Gong, Nanostructured materials for heterogeneous electrocatalytic CO_2 reduction and their related reaction mechanisms, Angew. Chem. Int. Ed. 56 (2017) 11326–11353.

[3] T.-Y. Chang, R.-M. Liang, P.-W. Wu, J.-Y. Chen, Y.-C. Hsieh, Electrochemical reduction of CO_2 by Cu_2O-catalyzed carbon clothes, Mater. Lett. 63 (2009) 1001–1003.

[4] E. Andrews, M. Ren, F. Wang, Z. Zhang, P. Sprunger, R. Kurtz, J. Flake, Electrochemical reduction of CO_2 at Cu nanocluster/(100) ZnO electrodes, J. Electrochem. Soc. 160 (2013) H841–H846.

[5] X. Sun, Q. Zhu, X. Kang, H. Liu, Q. Qian, Z. Zhang, B. Han, Molybdenum-bismuth bimetallic chalcogenide nanosheets for highly efficient electrocatalytic reduction of carbon dioxide to methanol, Angew. Chem. Int. Ed. 55 (2016) 6771–6775.

[6] J. Albo, A. Sáez, J. Solla-Gullón, V. Montiel, A. Irabien, Production of methanol from CO_2 electroreduction at Cu_2O and Cu_2O/ZnO-based electrodes in aqueous solution, Appl. Catal. B: Environ. 176–177 (2015) 709–717.

[7] H. Yang, Y. Wu, G. Li, Q. Lin, Q. Hu, Q. Zhang, J. Liu, C. He, Scalable production of efficient single-atom copper decorated carbon membranes for CO_2 electroreduction to methanol, J. Am. Chem. Soc. 141 (2019) 12717–12723.

[8] Q. Zhao, C. Zhang, R. Hu, Z. Du, J. Gu, Y. Cui, X. Chen, W. Xu, Z. Cheng, S. Li, B. Li, Y. Liu, W. Chen, C. Liu, J. Shang, L. Song, S. Yang, Selective etching quaternary MAX phase toward single atom copper immobilized MXene ($Ti_3C_2Cl_x$) for efficient CO_2 electroreduction to methanol, ACS Nano 15 (2021) 4927–4936.

[9] D. Xiang, D. Magana, R.B. Dyer, CO_2 reduction catalyzed by mercaptopteridine on glassy carbon, J. Am. Chem. Soc. 136 (2014) 14007–14010.

[10] J. Liu, D. Yang, Y. Zhou, G. Zhang, G. Xing, Y. Liu, Y. Ma, O. Terasaki, S. Yang, L. Chen, Tricycloquinazoline-based 2d conductive metal-organic frameworks as promising electrocatalysts for co2 reduction angew, Chem. Int. Ed. 60 (2021) 14473–14479.

[11] E. Boutin, M. Wang, J.C. Lin, M. Mesnage, D. Mendoza, B. Lassalle-Kaiser, C. Hahn, T.F. Jaramillo, M. Robert, Aqueous electrochemical reduction of carbon dioxide and carbon monoxide into methanol with cobalt phthalocyanine, Angew. Chem. Int. Ed. 58 (2019) 16172–16176.

[12] Y. Wu, Z. Jiang, X. Lu, Y. Liang, H. Wang, Domino electroreduction of CO_2 to methanol on a molecular catalyst, Nature 575 (2019) 639–642.

[13] S. Lin, C.S. Diercks, Y.B. Zhang, N. Kornienko, E.M. Nichols, Y. Zhao, A.R. Paris, D. Kim, P. Yang, O.M. Yaghi, C.J. Chang, Covalent organic frameworks comprising cobalt porphyrins for catalytic CO_2 reduction in water, Science 349 (2015) 1208–1213.

[14] X. Wang, Y. Pan, H. Ning, H. Wang, D. Guo, W. Wang, Z. Yang, Q. Zhao, B. Zhang, L. Zheng, M. Wu, Hierarchically micro- and meso-porous Fe-N_4O-doped carbon as robust electrocatalyst for CO_2 reduction, Appl. Catal. B: Environ. 266 (2020), 118630.

[15] L. Peng, Y. Wang, Y. Wang, N. Xu, W. Lou, P. Liu, D. Cai, H. Huang, J. Qiao, Separated growth of Bi-Cu bimetallic electrocatalysts on defective copper foam for highly converting CO_2 to formate with alkaline anion-exchange membrane beyond $KHCO_3$ electrolyte, Appl. Catal. B: Environ. 288 (2021), 120003..

[16] S. Gao, Y. Lin, X. Jiao, Y. Sun, Q. Luo, W. Zhang, D. Li, J. Yang, Y. Xie, Partially oxidized atomic cobalt layers for carbon dioxide electroreduction to liquid fuel, Nature 529 (2016) 68–71.

[17] Y. Hori, H. Wakebe, T. Tsukamoto, O. Koga, Electrocatalytic process of CO selectivity in electrochemical reduction of CO_2 at metal electrodes in aqueous media, Electrochim. Acta 39 (1994) 1833–1839.

[18] D. Kim, J. Resasco, Y. Yu, A.M. Asiri, P. Yang, Synergistic geometric and electronic effects for electrochemical reduction of carbon dioxide using gold-copper bimetallic nanoparticles, Nat. Commun. 5 (2014) 4948.

[19] Z. Gu, H. Shen, Z. Chen, Y. Yang, C. Yang, Y. Ji, Y. Wang, C. Zhu, J. Liu, J. Li, T.-K. Sham, X. Xu, G. Zheng, Efficient electrocatalytic CO_2 reduction to C2+ alcohols at defect-site-rich Cu surface, Joule 5 (2021) 429–440.

[20] Z.-Z. Wu, F.-Y. Gao, M.-R. Gao, Regulating the oxidation state of nanomaterials for electrocatalytic CO_2 reduction, Energy Environ. Sci. 14 (2021) 1121–1139.

[21] E. Boutin, L. Merakeb, B. Ma, B. Boudy, M. Wang, J. Bonin, E. Anxolabehere-Mallart, M. Robert, Molecular catalysis of CO_2 reduction: recent advances and perspectives in electrochemical and light-driven processes with selected Fe, Ni and Co aza macrocyclic and polypyridine complexes, Chem. Soc. Rev. 49 (2020) 5772–5809.

[22] X. Kong, Yan Liu, P. Li, J. Ke, Z. Liu, F. Ahmad, W. Yan, Z. Li, Z. Geng, J. Zeng, Coordinate activation in heterogeneous carbon dioxide reduction on Co-based molecular catalysts, Appl. Catal. B: Environ. 268 (2020), 118452.

[23] X. Kong, J. Ke, Z. Wang, Y. Liu, Y. Wang, W. Zhou, Z. Yang, W. Yan, Z. Geng, J. Zeng, Co-based molecular catalysts for efficient CO_2 reduction via regulating spin states, Appl. Catal. B: Environ. 290 (2021), 120067.

[24] H.B. Yang, S.-F. Hung, S. Liu, K. Yuan, S. Miao, L. Zhang, X. Huang, H.-Y. Wang, W. Cai, R. Chen, J. Gao, X. Yang, W. Chen, Y. Huang, H.M. Chen, C.M. Li, T. Zhang, B. Liu, Atomically dispersed Ni(I) as the active site for electrochemical CO_2 reduction, Nat. Energy 3 (2018) 140–147.

[25] Z. Liang, H.Y. Wang, H. Zheng, W. Zhang, R. Cao, Porphyrin-based frameworks for oxygen electrocatalysis and catalytic reduction of carbon dioxide, Chem. Soc. Rev. 50 (2021) 2540–2581.

[26] N. Han, Y. Wang, L. Ma, J. Wen, J. Li, H. Zheng, K. Nie, X. Wang, F. Zhao, Y. Li, J. Fan, J. Zhong, T. Wu, D.J. Miller, J. Lu, S.-T. Lee, Y. Li, Supported cobalt polyphthalocyanine for high-performance electrocatalytic CO_2 reduction, Chem 3 (2017) 652–664.

[27] X. Zhang, Z. Wu, X. Zhang, L. Li, Y. Li, H. Xu, X. Li, X. Yu, Z. Zhang, Y. Liang, H. Wang, Highly selective and active CO_2 reduction electrocatalysts based on cobalt phthalocyanine/carbon nanotube hybrid structures, Nat. Commun.. 8 (2017) 14675.

[28] J. Su, J.-J. Zhang, J. Chen, Y. Song, L. Huang, M. Zhu, B.I. Yakobson, B.Z. Tang, R. Ye, Building a stable cationic molecule/electrode interface for highly efficient and durable CO_2 reduction at an industrially relevant current, Energy Environ. Sci. 14 (2021) 483–492.

[29] Y. Liu, S. Li, L. Dai, J. Li, J. Lv, Z. Zhu, A. Yin, P. Li, B. Wang, The synthesis of hexaazatrinaphthylene-based 2d conjugated copper metal-organic framework for highly selective and stable electroreduction of CO_2 to methane, Angew. Chem. Int. Ed. 60 (2021) 16409–16415.

[30] P. Shao, W. Zhou, Q. Hong, L. Yi, L. Zheng, W. Wang, H. Zhang, H. Zhang, J. Zhang, Synthesis of a boron-imidazolate framework nanosheet with dimer copper units for CO_2 electroreduction to ethylene, Angew. Chem. Int. Ed. 60 (2021) 16687–16692.

[31] H.J. Zhu, M. Lu, Y.R. Wang, S.J. Yao, M. Zhang, Y.H. Kan, J. Liu, Y. Chen, S.L. Li, Y. Q. Lan, Efficient electron transmission in covalent organic framework nanosheets for highly active electrocatalytic carbon dioxide reduction, Nat. Commun. 11 (2020) 497.

[32] B. Han, X. Ding, B. Yu, H. Wu, W. Zhou, W. Liu, C. Wei, D. B.g Chen, H. Qi, K. Wang, Y. Wang, B. Chen, J. Jiang, Two-dimensional covalent organic frameworks with cobalt(ii)-phthalocyanine sites for efficient electrocatalytic carbon dioxide reduction, J. Am. Chem. Soc. 18 (2021) 7104–7113.

[33] X. Zhang, Y. Wang, M. Gu, M. Wang, Z. Zhang, W. Pan, Z. Jiang, H. Zheng, M. Lucero, H. Wang, G.E. Sterbinsky, Q. Ma, Y.-G. Wang, Z. Feng, J. Li, H. Dai, Y. Liang, Molecular engineering of dispersed nickel phthalocyanines on carbon nanotubes for selective CO_2 reduction, Nat. Energy 5 (2020) 684–692.

[34] X. Wang, Z. Chen, X. Zhao, T. Yao, W. Chen, R. You, C. Zhao, G. Wu, J. Wang, W. Huang, J. Yang, X. Hong, S. Wei, Y. Wu, Y. Li, Regulation of coordination number over single Co sites: triggering the efficient electroreduction of CO_2, Angew. Chem. Int. Ed. 57 (2018) 1944–1948.

[35] S.J. Lyle, T.M. Osborn Popp, P.J. Waller, X. Pei, J.A. Reimer, O.M. Yaghi, Multistep solid-state organic synthesis of carbamate-linked covalent organic frameworks, J. Am. Chem. Soc. 28 (2019) 11253–11258.

[36] Kurt A.W. Wallenfels, Wilfried J. Draber, Darstellung von tetraamino-benzochinon-1,4 aus fluoranil und chloranil, Tet. Lett 13 (1959) 24–25.

[37] Z. Luo, L. Liu, J. Ning, K. Lei, Y. Lu, F. Li, J. Chen, A. Microporous, Covalent-organic framework with abundant accessible carbonyl groups for lithium-ion batteries, Angew. Chem. Int. Ed. 57 (2018) 9443–9446.

[38] R. Manivannan, S. Ciattini, L.C. Kuppanagounder, P. Elango, Benzoquinone-imidazole hybrids as selective colorimetric sensors for cyanide in aqueous, solid and gas phases, RSC Adv. 5 (2015) 87341–87351.

[39] S. Stang, A. Lebkücher, P. Walter, E. Kaifer, H.J. Himmel, Redox-active guanidine ligands with pyridine and p-benzoquinone backbones, Eur. J. Inorg. Chem. 30 (2012) 4833–4845.

[40] T. Li, W.-D. Zhang, Y. Liu, Y. Li, C. Cheng, H. Zhu, X. Yan, Z. Li, Z.-G. Gu, A two-dimensional semiconducting covalent organic framework with nickel(ii) coordination for high capacitive performance, J. Mater. Chem. A 7 (2019) 19676–19681.

[41] Y. Wang, H. Lei, S. Lu, Z. Yang, B. Xu, L. Xing, X. Liu, Cu_2O nano-flowers/graphene enabled scaffolding structure catalyst layer for enhanced CO_2 electrochemical reduction, Appl. Catal. B: Environ. 305 (2022), 121022.

[42] G. Kresse, J. Furthmüller, Efficient iterative schemes for ab initio totalenergy calculations using a plane-wave basis set, Phys. Rev. B 54 (1996) 11169–11186.

[43] G. Kresse, J. Furthmüller, Efficiency of ab-initio total energy calculations for metals and semiconductors using a plane-wave basis set, Comput. Mater. Sci. 61 (1996) 15–50.

[44] C. Adamo, V. Barone, Toward reliable density functional methods without adjustable parameters: the PBE0 model, J. Chem. Phys. 110 (1999) 6158–6170.

[45] B. Ravel, M. Newville, ATHENA, ARTEMIS, HEPHAESTUS: data analysis for X-ray absorption spectroscopy using IFEFFIT, J. Synchrotron Rad. 12 (2005) 537–541.

[46] M. Newville, IFEFFIT: interactive XAFS analysis and FEFF fitting, J. Synchrotron Rad. 8 (2001) 322–324.

[47] J.J. Rehr, J. Mustre de Leon, S.I. Zabinsky, R.C. Albers, Theoretical x-ray absorption fine structure standards, J. Am. Chem. Soc. 113 (1991) 5135–5140.

[48] B.P. Biswal, S. Chandra, S. Kandambeth, B. Lukose, T. Heine, R. Banerjee, Mechanochemical synthesis of chemically stable isoreticular covalent organic frameworks, J. Am. Chem. Soc. 135 (2013) 5328–5331.

[49] L. Wang, L. Ni, X. Hou, L. Chen, F. Li, J. Chen, A. Two-Dimensional, Metal-organic polymer enabled by robust nickel-nitrogen and hydrogen bonds for exceptional sodium-ion storage, Angew. Chem. Int. Ed. 59 (2020) 22126–22131.

[50] Z. Liang, D. Jiang, X. Wang, M. Shakouri, T. Zhang, Z. Li, P. Tang, L. Jordi. Llorca, Y. Liu, M. Yuan, R.E. Heggen, J.R. Dunin-Borkowski, A. Morante, J. Cabot, Arbiol, Molecular engineering to tune the ligand environment of atomically dispersed nickel for efficient alcohol electrochemical oxidation, Adv. Funct. Mater. 31 (2021), 2106369.

[51] Y. Ni, L. Lin, Y. Shang, L. Luo, L. Wang, Y. Lu, Y. Li, Z. Yan, K. Zhang, F. Cheng, J. Chen, Regulating electrocatalytic oxygen reduction activity of a metal coordination polymer via d-π conjugation, Angew. Chem. Int. Ed. 60 (2021) 16937–16941.

[52] J. Gu, C.-S. Hsu, L. Bai, H.M. Chen, X. Hu, Atomically dispersed Fe3+ sites catalyze efficient CO_2 electroreduction to CO, Atomically dispersed Fe3+ sites catalyze efficient CO2 electroreduction to CO, Science 364 (2019) 1091–1094.

[53] J. Wang, H. Yang, Q. Liu, Q. Liu, X. Li, T. Cheng, H.B. Wu, Fastening Br⁻ ions at copper–molecule interface enables highly efficient electroreduction of CO_2 to ethanol, ACS Energy Lett. 6 (2021) 437–444.